Quantum Interference of Electromechanically Stabilized Emitters in Nanophotonic Devices

B. Machielse,[1,*] S. Bogdanovic,[2,*] S. Meesala,[2,*] S. Gauthier,[3] M. J. Burek,[2] G. Joe,[2] M. Chalupnik,[1] Y. I. Sohn,[2]
J. Holzgrafe,[2] R. E. Evans,[1] C. Chia,[2] H. Atikian,[2] M. K. Bhaskar,[1] D. D. Sukachev,[1,4] L. Shao,[2]
S. Maity,[2] M. D. Lukin,[1] and M. Lončar[2,†]

[1]*Department of Physics, Harvard University, Cambridge, Massachusetts 02138, USA*
[2]*John A. Paulson School of Engineering and Applied Sciences, Harvard University,
Cambridge, Massachusetts 02138, USA*
[3]*Department of Physics and Astronomy, University of Waterloo, 200 University Avenue,
West Waterloo, Ontario N2L 3G1, Canada*
[4]*P.N. Lebedev Physical Institute of the RAS, Moscow 119991, Russia*

Photon-mediated coupling between distant matter qubits may enable secure communication over long distances, the implementation of distributed quantum computing schemes, and the exploration of new regimes of many-body quantum dynamics. Solid-state quantum emitters coupled to nanophotonic devices represent a promising approach towards these goals, as they combine strong light-matter interaction and high photon collection efficiencies. However, nanostructured environments introduce mismatch and diffusion in optical transition frequencies of emitters, making reliable photon-mediated entanglement generation infeasible. Here we address this long-standing challenge by employing silicon-vacancy color centers embedded in electromechanically deflectable nanophotonic waveguides. This electromechanical strain control enables control and stabilization of optical resonance between two silicon-vacancy centers on the hour timescale. Using this platform, we observe the signature of an entangled, superradiant state arising from quantum interference between two spatially separated emitters in a waveguide. This demonstration and the developed platform constitute a crucial step towards a scalable quantum network with solid-state quantum emitters.

Subject Areas: Optics, Photonics, Quantum Information

I. INTRODUCTION

Solid-state emitters with inversion symmetry [1] are promising for use in optical quantum networks [2–5] due to their ability to be integrated into nanophotonic devices [6–9]. These emitters have suppressed static electric dipole moments, decreasing the susceptibility of their optical transition frequencies to fluctuations of electric fields that occur near device surfaces [1,8,10]. This fundamental property has been leveraged most notably with the negatively charged silicon-vacancy (SiV) center in diamond to achieve emitter-photon interaction with cooperativity greater than 20 in nanophotonic cavities [9]. The platform developed around this color center also provides other essential components for quantum networking, such as a

long-lived quantum memory [7] and efficient photon collection [11].

Nevertheless, in terms of advancing towards multiqubit networks, even inversion-symmetric and other electric field insensitive [12–14] emitters present challenges when incorporated into nanophotonic devices. They exhibit a significant inhomogeneous distribution of their optical transition frequencies as well as residual instability in the form of spectral diffusion [1,8]. Demonstrating full control of their spectral behavior is necessary to generate mutually indistinguishable photons, the key ingredient for long-distance entanglement [10,15]. Because these emitters cannot be spectrally tuned using electric fields, the established tuning mechanism for solid-state emitters [10,16], previous experiments involving indistinguishable photon generation from such defects have relied on Raman [6,17] and magnetic field [9] tuning. However, these techniques constrain either the spin or optical degree of freedom of the color center and are challenging to implement in the multiqubit regime.

Inspired by experiments involving semiconductor quantum dots [18,19], initial experiments with diamond cantilevers have demonstrated the capacity to tune single SiV

centers using strain [20,21]. However, the suitability of this approach for photon-mediated entanglement of multiple emitters remains an open question. In this work, we show that strain control can be used to manipulate the optical resonances of solid-state emitters and generate quantum interference between them. The demonstrated integration of strain control with nanophotonic devices represents a key step towards the realization of scalable quantum networks.

II. WAVEGUIDES WITH STRAIN CONTROL

Our devices, presented in Fig. 1, consist of triangular cross-section waveguides fabricated from single-crystal diamond [22,23] (see Appendix A). Each of these waveguides is connected to a support structure on one end [Fig. 1(b)]. The other end is tapered to allow for collection of photons from the waveguide into an optical fiber with better than 85% efficiency [11] [Fig. 1(c)]. In order to
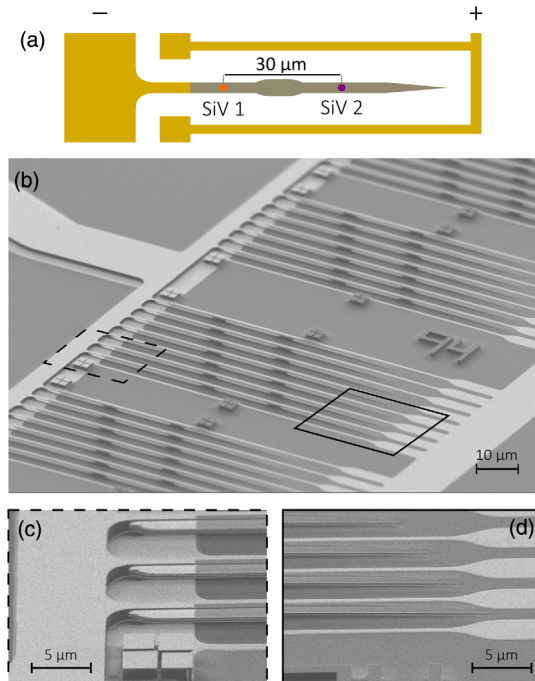
embed SiV centers within diamond nanophotonic devices, we adapt a masked implantation technique previously used for bulk substrates [24]. We implant silicon ions at a density of 2×10^{12} ions/cm^2, a density similar to that used for cavity QED experiments [9]. After the creation of SiV centers, gold electrodes are patterned onto the devices such that metallized parts of the waveguide act as one plate of a capacitor, with the other plate located on the diamond substrate [Fig. 1(b)]. Applying a voltage difference to these plates generates a force that deflects a portion of the waveguide, applying electrically controllable strain to the embedded SiV centers. This strain field perturbs the diamond lattice around the SiV, which shifts the Coulomb energy of the orbitals and tunes the frequency of the optical transitions [1].

We measure the strain response of two SiV centers 30 μm apart within the same diamond device by resonantly exciting their optical transitions and collecting their phonon-sideband (PSB) emission at 4 K (Fig. 2). The difference in the position of SiV centers in the device accounts for the difference in their response to the applied voltage [21], allowing us to overlap their optical transitions (Fig. 2, left hand and right hand inset). The waveguide supports [Fig. 1(a), rounded gray region] between the SiV centers act as a mechanical clamp

FIG. 1.   Schematic of diamond nanophotonics device. (a) Diamond waveguides (gray) are implanted with color centers (purple and orange) at desired locations on the device. Electrodes (gold) are used to define a capacitor between plates located on the device (negative terminal) and below the device (positive terminal). Applying bias voltage between the plates causes the deflection of the doubly clamped cantilever. This tunes color centers between the plates and the first clamp (orange circle) without perturbing color centers beyond the clamp (purple circle). (b) Scanning electron micrograph (SEM) of the photonic devices. (c) Capacitor plates located on and below the devices. (d) Diamond tapers used to extract photons from waveguides. This enables the extraction efficiency of more than 85% from the diamond waveguide into the fiber.
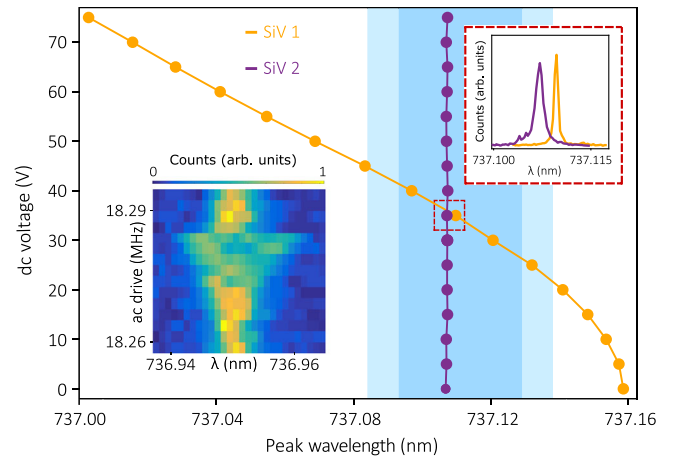

FIG. 2.   Characterization of dc and ac voltage response of the devices. Voltage bias is applied to the capacitor plates, resulting in strain fields that tune the optical transitions of SiV1 in the deflected portion of the device (orange) compared to the optical transitions of SiV2 in the stationary regions (purple). The tuning range of the SiV color center greatly exceeds the inhomogeneous distribution for 50% (75%) of SiV color centers observed in this experiment shown in dark (light) blue shading. The right-hand inset shows the photoluminescence excitation spectra of two color centers at a voltage near the overlap. The left-hand inset shows the ac response of the cantilever system, measured by observing SiV optical transitions while modulating the ac driving frequency. Driving the cantilever resonance with its mechanical mode results in linewidth broadening of the color center optical transitions.

preventing strain from propagating and impacting the spectral behavior of color centers in the portion of the waveguide beyond the clamp. We observe a tuning range of over 80 GHz (150 pm), a factor of 3 larger than the total inhomogeneous distribution of the SiV optical transitions measured in these devices (Fig. 2, blue shaded region). This is sufficient range to completely eliminate the effects of static strain variations on SiV optical transitions.

To determine the bandwidth of our electromechanical actuation scheme, we investigate a SiV color center's spectral response to ac mechanical driving of the nanophotonic structure (Fig. 2, blue inset). We apply a dc bias combined with a variable-frequency rf signal to the gold electrodes and monitor the SiV optical transition. When the rf drive frequency matches one of the nanobeam's mechanical modes, we observe linewidth broadening of the SiV coupled to this mechanical mode due to the resonant amplification of the driving signal [25]. Using this technique, we observe and drive modes with mechanical frequencies of up to 100 MHz. Optimizing the device design could enable the electromechanical driving of vibrational modes with gigahertz frequencies which are resonant with SiV spin transitions. This could open new possibilities for engineering coherent spin-phonon interactions [20].

III. MITIGATION OF SPECTRAL DIFFUSION

The high bandwidth of our electromechanical actuation scheme is sufficient to suppress spectral diffusion exhibited by the SiV center [8]. Monitoring a SiV center's optical transition over the course of five hours, we observe spectral diffusion that is an order of magnitude larger than its single-scan linewidth of around 300 MHz [Fig. 3(a)]. Using a pulsed feedback scheme that applies a voltage adjustment every 20 sec, we reduce the total summed linewidth by almost an order of magnitude on a timescale of several hours [Fig. 3(b)]. The efficacy of this feedback scheme is limited by the long duration of the laser scan used to capture the full extent of the spectral diffusion. This results in imperfect locking of the SiV optical transition to the target frequency (see Appendix C). The bandwidth of this spectral stabilization technique is improved by performing a faster 5 Hz sweep around a narrower region around the position of the SiV center optical transition. We monitor the noise spectrum of the SiV center emission with and without a lock-in feedback scheme applied to the device voltage [Fig. 3(c)]. The application of feedback results in an intensity noise reduction by approximately 8 dB, consistent with the stabilization achieved in Fig. 3(b). We attribute the frequency component dominated by the $1/f$ noise to slow strain fluctuations and second-order susceptibility to electric field fluctuations in the SiV environment. Beyond this regime, our feedback scheme is limited by photon shot noise [Fig. 3(c)]. Further improving the SiV count rate
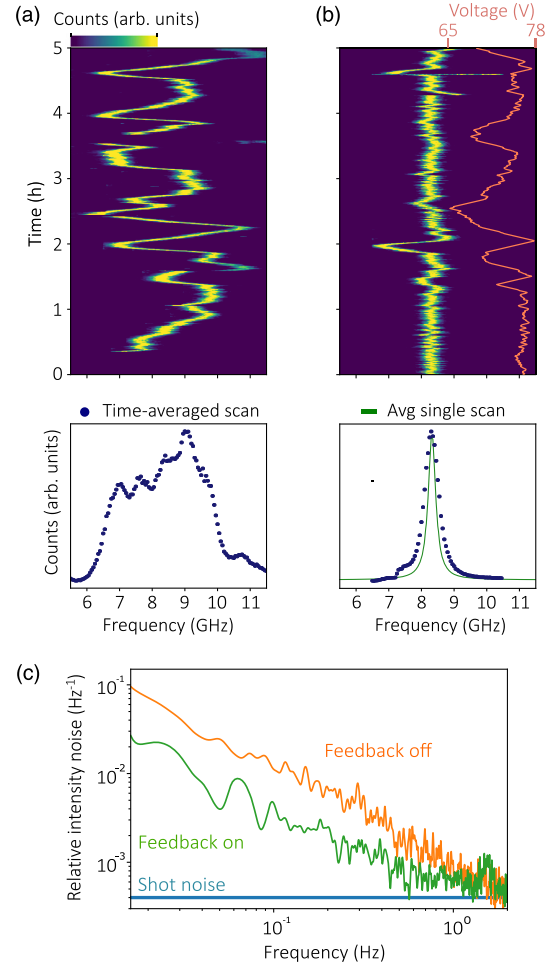

FIG. 3. Reduction of spectral diffusion using nanomechanical strain. (a) Top: Spectral diffusion of SiV center optical transition, measured over a 5-h period. Bottom: Time-averaged spectrum over the same period. (b) Top: Measurement of the SiV spectral diffusion with 20-sec pulsed feedback over a 5-h period. Bottom: Time-averaged spectra over a 5-h period (blue dots) show the reduction of total linewidth down to 500 MHz. The average of single-scan SiV linewidths is 350 MHz (green line). (c) Power spectral density of measured SiV count fluctuations with (without) feedback is presented by the green (orange) line, showing reduction of noise by an average of 8 dB. Blue line indicates statistical noise limit set by finite photon emission and collection rate.

through Purcell enhancement using a cavity could enable higher frequency feedback, as the existing scheme uses only a small share of the available actuation bandwidth.

IV. OBSERVATION OF QUANTUM INTERFERENCE

With the optical transitions of the SiV centers tuned and stabilized, we proceed to generate probabilistic entanglement between two color centers. We begin by using strain control to set the optical transition frequencies between the
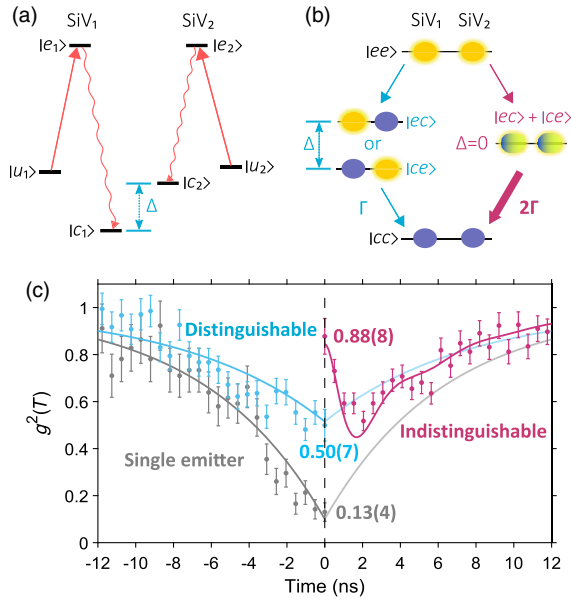
FIG. 4. Observation of the superradiant entangled state using strain control. (a) Level structure for two SiV centers. Strain tuning of one SiV color center changes the detuning (Δ) between their $|e\rangle$ to $|c\rangle$ transitions. Separate lasers are applied to excite the $|u\rangle$ to $|e\rangle$ transition of each emitter. (b) A single photon emitted from the two excited emitters with distinguishable transitions ($\Delta \neq 0$) projects the system to a statistical mixture of $|ec\rangle$ and $|ce\rangle$ states (blue decay path). When the emitters are indistinguishable ($\Delta = 0$), the emission of one photon projects the system into a superradiant bright state (purple decay path) that decays at a rate 2 times faster than that of the statistical mixture. (c) The second-order photon correlation function is measured for a single emitter (left-hand panel, gray data points) and for two spectrally distinguishable emitters (left-hand panel, blue data points). Measured $g^{(2)}(0)$ is 0.13(4) and 0.50(7) for the single emitter and distinguishable cases, respectively. Exponential curves fit to the data are plotted and mirrored onto the right half of the plot (gray and blue lines). For two emitters tuned into resonance, we observe the generation of a superradiant entangled state, signified by the peak in the photon correlation (right-hand panel, purple data points). Data are overlaid with a simulated model with a single fit parameter (see Appendix D). For indistinguishable emitters, we measure $g^{(2)}(0) = 0.88(8)$, limited primarily by detector jitter.

lower branch of the ground state ($|c\rangle$) and the excited state ($|e\rangle$) of two emitters at the target detuning (Δ) by applying the appropriate voltage [Fig. 4(a)]. The transitions between the upper branch of the ground state ($|u\rangle$) and the excited state ($|e\rangle$) of the two emitters are then continuously excited using two separate lasers [Fig. 4(a)]. Finally, the photons emitted into the diamond waveguide are collected through a tapered fiber interface and filtered using a high-finesse Fabry-Perot filter (see Appendix B) in order to separate the desired optical transition from the excitation laser [6].

We characterize our setup by measuring the second-order correlation function between photons from a single

excited SiV center [Fig. 4(c), left-hand panel]. We observe the suppression of photon coincidences with $g^{(2)}_{\text{single}}(0) = 0.13(4)$, a quantity raised above its ideal value of 0 by dark counts of the photon detectors. Next, we simultaneously excite both SiV centers and measure their photon correlation function. When two excited SiV centers are spectrally detuned ($\Delta \neq 0$), their emitted photons are distinguishable and the detection of the first photon projects the system into the statistical mixture of the $|ce\rangle$ and $|ec\rangle$ states [Fig. 4(b), blue path] [6]. In this case, the zero-time-delay photon correlation function reaches $g^{(2)}_{\text{dist}}(0) = 0.50(7)$ [Fig. 4(c), left-hand panel].

When the two SiV optical transitions are tuned into resonance ($\Delta = 0$), detection of the first emitted photon from a pair of excited SiV color centers projects the system into an entangled, bright state [Fig. 4(b), red path]. This results from the indistinguishability of the emitted photons, which eliminates the information about which SiV produced the photon. This bright state is identified by the superradiant emission of a second photon at twice the rate expected compared to the distinguishable case [6,26]. This increased emission rate results in an increased probability of observing photon coincidences—resulting in the creation of a peak in $g^{(2)}(0)$. We confirm the generation of an entangled state by observing this superradiant peak in the photon correlation function [Fig. 4(c), right-hand panel] with $g^{(2)}_{\text{ind}}(0) = 0.88(8)$. Experimental results are in good agreement with a simulated model of our system [Fig. 4(c), red curve], which uses only a single fitting parameter, the phonon-induced mixing rate between the $|u\rangle$ and $|c\rangle$ ground states [27] (see Appendix D). Using the height of the superradiant peak and the value of the $g^{(2)}_{\text{single}}$, we calculate a lower bound on the conditional bright-state fidelity to be 0.8(1), indicating the observation of an entangled state [6] (see Appendix E).

In particular, the $g^{(2)}$ data presented in the right-hand panel of Fig. 4 can be understood as consisting of two parts. First, the dip with a decay timescale of about 10 ns occurs because photons collected in this experiment can only be generated from the $|e\rangle$ state, and the detection of a photon leads to projection of the system into the $|c\rangle$ state. The timescale of the dip then corresponds to the average amount of time between the emitter arriving in the $|c\rangle$ state and it being excited to the $|e\rangle$ state. This timescale is primarily set by the ground-state mixing rate between $|c\rangle$ and $|u\rangle$ states in our experiment, but in cases of low laser driving power can also be broadened by the slow Rabi driving between the $|e\rangle$ and $|u\rangle$ states. The second feature is the superradiant peak. Theoretically, the width of this peak should be set to roughly 1 ns (half of the excited state lifetime), as superradiant effects should dominate at this timescale. In reality, both the electronic jitter and the laser power impact the measured width. The total electronic jitter measured in our detection electronics is 350 ps, a timescale comparable to

the anticipated peak timescale of 1 ns, leading to broadening of the measured feature (see Appendix D). Fast laser driving could also reduce the timescale of the peak by providing another driven decay channel (stimulated emission) from the bright state. The oscillations in the $g^{(2)}$ for indistinguishable emitters result from a combination of small mismatch between emitter optical transitions and Rabi driving between the $|u\rangle$ and $|e\rangle$ states in line with the theory.

V. CONCLUSION AND DISCUSSION

In conclusion, we show a scalable approach to generating quantum interference between solid-state emitters in nanophotonic devices using strain. Using our electromechanically controlled strain field, we realize a reduction of spectral diffusion by almost an order of magnitude over a broad bandwidth and achieve a spectral tuning range exceeding 150 pm (80 GHz), several times greater than the SiV inhomogeneous distribution inside nanophotonic devices. This approach can be directly adapted to other quantum emitters such as quantum dots, other inversion-symmetric color centers in diamond with higher quantum efficiency [28], as well as other electric field insensitive emitters [12]. Furthermore, high-frequency strain control inside a nanophotonic cavity can lead to a photon- or phonon-mediated gate between quantum memories [9,29,30]. By combining long-lived quantum memories with a high cooperativity nanophotonic interface and a direct mechanism for ensuring optical indistinguishability, the SiV platform fulfills the requirements for a scalable quantum network node and paves the way for realization of large-scale quantum networks.

APPENDIX A: DEVICE FABRICATION

This appendix describes the fabrication of the nanophotonic devices presented in Fig. 1 of the main text. The device fabrication presented in Fig. 5 is based on the techniques developed in Refs. [22,23,31]. The fabrication scheme for cantilever deflection is based on Ref. [21].

Single-crystal diamond substrates were obtained from element 6 (CVD grown, <5 ppb [N]). The substrates were mechanically polished, cleaned with a boiling 1:1:1 mixture of sulfuric acid, nitric acid, and perchloric acid (hereafter referred to as a triacid clean), and etched using the argon-chlorine etch (Unaxis Shuttleline ICP-RIE) to ensure maximum substrate smoothness.

We prepared the diamonds for fabrication of the photonic devices using a piranha and hydrofluoric acid clean. A 10 nm stiction layer of titanium was deposited using electron-beam evaporation, followed by spin coating with Hydrogen silsesquioxane resist (FOx-16, Dow Corning) diluted in methyl isobutyl ketone (MIBK) (Fig. 5, step 1). This resist was then exposed using electron-beam lithography and developed in 25% Tetramethylammonium hydroxide (Sigma-Aldrich). This was followed by a reactive-ion etch (RIE) using an argon-chlorine mixture to remove exposed titanium, followed by an oxygen RIE (Unaxis Shuttleline ICP-RIE), which transfers the mask pattern into diamond (Fig. 5, step 2). The ridge waveguides are transformed into freestanding triangular cross-section waveguides using an oxygen etch at an angle of 40 deg from the normal using an ion beam etcher (IBE) (Intlvac
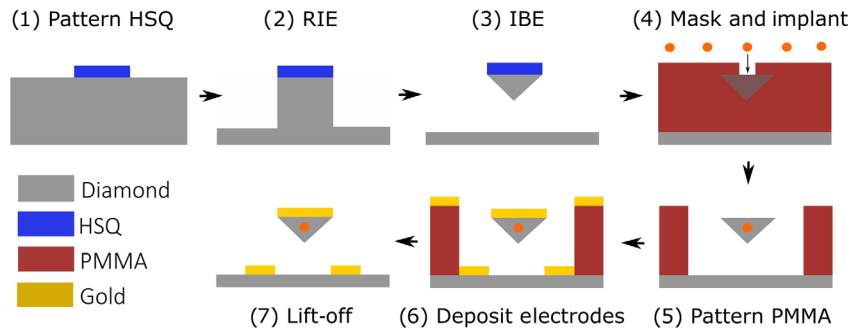
FIG. 5. Schematic of nanofabrication process. Diamond waveguides are fabricated using top-down and angled etching technique into the diamond substrate [22,23,31]. This was followed by patterning apertures on top of the fabricated structures through which Si + ions can reach the diamond substrate at desired locations [21]. Finally, we deposit gold electrodes on top of and below the diamond devices [11,32], which serve to deflect fabricated waveguides when a voltage is applied between them.

Nanoquest II) (Fig. 5, step 3). The etch mask was removed with a hydrofluoric acid clean, and the devices were dried in a critical point dryer.

In order to prepare the diamonds for implantation, the devices were again cleaned using piranha and hydrofluoric acid and then repeatedly spin coated with PMMA C4 (MicroChem) resist and a single layer of espacer 300Z (Showa Denko America), which served as a conductive layer. A multistep electron-beam alignment procedure was then used to align to markers etched into the diamond and expose the desired implantation spots. Devices were rinsed in water and then developed in a mixture of MIBK and isopropyl alcohol for 60 sec. The PMMA-coated devices were then sent for implantation with silicon ions (Innovion) (Fig. 5, step 4) with the desired dose and implantation energy calculated using SRIM simulation [32]. This method, inspired by previous work in the nitrogen vacancy center community [24], can be executed using standard electron-beam lithography tools, greatly increasing the accessibility of the SiV platform, which previously required specialized focused ion beam tools for implantation. Additionally, the same technique can be used to implant a variety of color centers into patterned substrates. The diamonds were then triacid cleaned, annealed at 1200 °C, and triacid cleaned again in order to turn implanted Si ions into SiV centers while removing damaged diamond from the surface of the devices. Creation of implanted SiV color centers was verified with a room-temperature confocal microscope.

The final step in device preparation was the patterning of electrodes. The devices were acid cleaned and coated with layers of MMAEL11 (MicroChem) and PMMA C4 (MicroChem), patterned using ebeam lithography (Fig. 5, step 5), and then coated with a 10 nm thin layer of titanium followed by roughly 100 nm layers of gold using an electron beam evaporator system (Fig. 5, step 6). Lift-off was then performed using heated Remover PG (MicroChem) (Fig. 5, step 7), leaving deposited gold electrodes on top of and below the fabricated nanostructures. Wire bonding to the millimeter-scale bonding pads provided leads through which voltage could be applied to the capacitor plates.

Fabrication of the tapered fibers followed the procedure documented in Ref. [11]. Thorlabs S630HP fibers were stripped of cladding and dipped into piranha using a home-built dip coater. A bath of hydrofluoric acid covered in a layer of o-xylene (Sigma-Aldrich) was prepared and the fibers were dipped into this mixture. By controlling the rate of the fiber extraction from this mixture, we were able to control the angle of the fiber taper which optimizes the efficiency of photon extraction from the diamond devices. During experiments, the tapered diamond end is brought into contact with a tapered optical fiber using a nanopositioning stage. Once contacted, we achieve adiabatic transfer of photons from the diamond waveguide into the optical fiber with efficiency greater than 85%.

APPENDIX B: SETUP

The experiment was carried out using a closed-cycle 4 K helium cryostat (Fusion F2 Montana Instruments). The layout of the setup is shown in Fig. 6. The position of the sample and the tapered fiber were controlled independently with two stacks of three-axis nanopositioning stages (Attocube, 2x ANP X101 and 1x z102 each) controlled with piezocontrollers (ANC 300 and ANC 350, respectively). Strain was applied to the sample nanobeams by applying a voltage difference (from 0 to 100 V) between two gold capacitor plates (Keithley Series 22020 voltage source). During experiments the leakage current resulting from 100 V applied bias was observed to be less than 50 nA, corresponding to less than 5 μW of heating. Based on COMSOL (COMSOL Inc.) simulations, we estimate that the electric field at the SiV location is less than 10^4 V/m. From the SiV transition dipole moment of 14D [33], we calculate that this corresponds to a second-order Stark shift of roughly 1 MHz.

To allow for the independent excitation of spatially separated SiV centers, we set the location of the two independent excitation positions using two scanning mirrors (Newport FSM300 and Mad City Labs MCLS02813). We periodically pulsed a green laser (Thorlabs LP520 nm) to repump our SiV centers into the negative charge state. This laser was run at a power of 10 μW on a 10% duty cycle. For identifying the location of the SiV centers within the diamond waveguide, an off-resonant 700 nm laser (Thorlabs M700F3) was scanned along the waveguide and the color center's zero-phonon line (ZPL) emission was collected via free space using an avalanche photodiode (APD) (4X Perkin Elmer SPCM-AQRH-14-FC). Resonant excitation of SiV centers was performed using a continuous wave tunable Ti:sapphire laser (M-Squared SolsTiS-2000-PSX-XF) and a home-built external-cavity diode laser (Opnext Diode HL7302MG, Littrow configuration), and the longer wavelength SiV phonon-sideband emission was collected using a free-space APD. Fast modulation of the Ti:sapphire laser sideband used in the feedback schemes described in Fig. 3 was performed by sending the laser through an electro-optic modulator (EOM) (iXBlue photonics NIR MX800) with a microwave (MW) frequency modulation input (HP 83711B, capable of operating up to 20 GHz).

A significant part of the SiV emission coupled to the diamond waveguide mode and was collected by a tapered optical fiber (collection efficiency of about 85%). This emission was then launched into free space and sent through a homemade, tunable, high-finesse (500 MHz linewidth, 150 GHz free spectral range) Fabry-Perot cavity frequency filter. This filter separated the SiV fluorescence from excitation laser photons scattered into the waveguide.

In the experiment involving two emitters (Fig. 4), this frequency filter was used to guarantee successful spectral overlap of the two SiV center's emission lines. Their
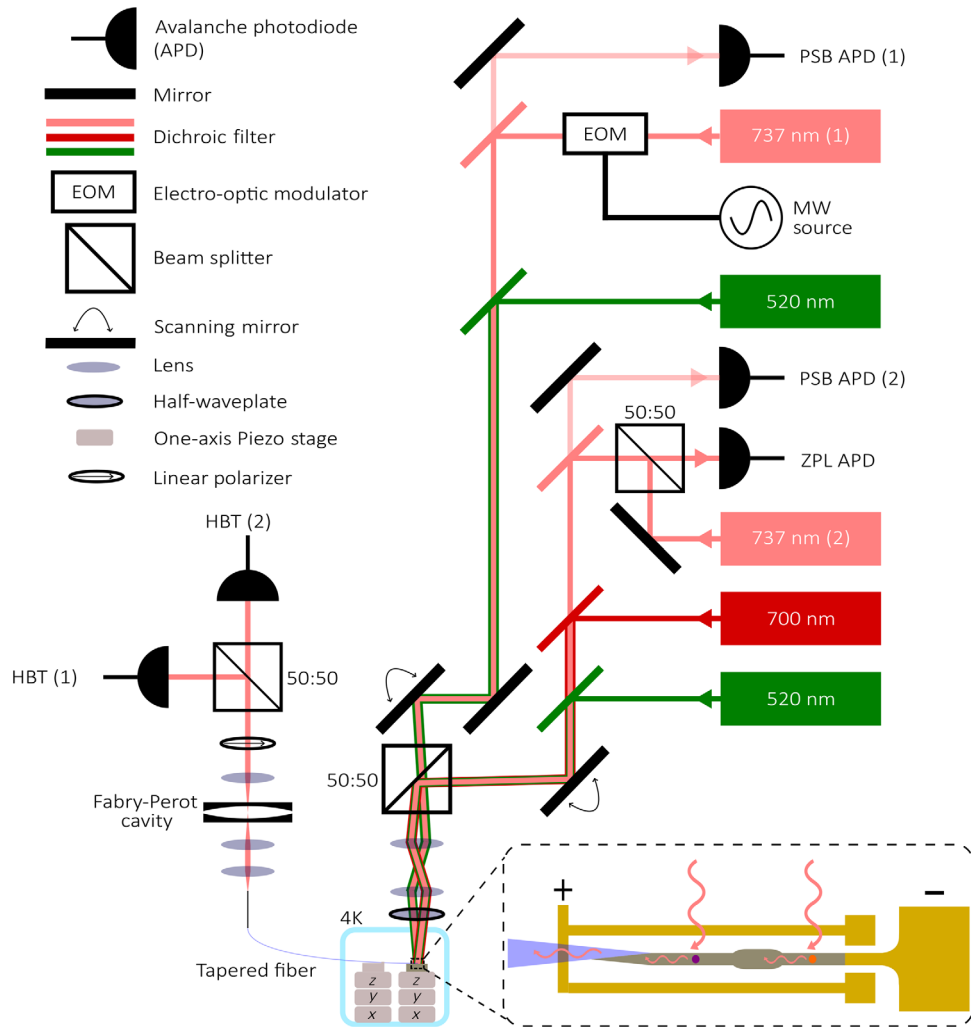
FIG. 6.   Overview of the setup used in this experiment.

emission then passed through a linear polarizer which erased any polarization mismatch (containing which-path information) between the two emitters, followed by a Hanbury–Brown Twiss (HBT) interferometer consisting of a 50∶50 beam splitter (fiber coupled) with equal arm lengths and two APDs. A time correlator (Picoharp PH300) connected to the two APDs of the HBT interferometer was then used to measure the second-order photon correlation function.

The photon correlation function of indistinguishable emitters [Fig. 4(c), right-hand panel] was obtained by programming the automatic start of the 0.5-sec-long measurement sequence conditioned on the APD count rate passing the set threshold value. This threshold value ensured that the photons emitted from both SiV centers passed through the Fabry-Perot cavity, which signified that their optical transitions were on resonance and the emitted photons were indistinguishable. In the case of the count rate dropping below the threshold value, strain would be applied until the count rate through the cavity filter was again maximized and the experiment would

proceed. This mechanism also stopped the experiment when mechanical drift of the Fabry-Perot cavity or the optical alignment decreased the measured count rate. In all, we estimate that the total duty cycle of our experiment was 45.3%, limited primarily by instability of the Fabry-Perot cavity. In the experiment measuring the photon correlation function of distinguishable emitters [Fig. 4(c), left-hand panel], this overlap was not ensured and the polarizer was removed from the beam path, making the emitted photons distinguishable.

APPENDIX C: FEEDBACK SCHEME

In order to lock a SiV optical transition to a target wavelength, two different feedback schemes were used.

In the first scheme, chosen to give visual demonstration of the efficacy of the strain-tuning technique, we collected SiV phonon-sideband emission produced during a 20-sec-long laser scan to extract information about the optical transition frequency. The resulting absorption profile was then fit using a Lorentzian with 3 fitting parameters, accounting for the

peak wavelength, amplitude, and width of the SiV spectral line. A single voltage step was then executed to move the peak wavelength of the spectral line towards the target value, after which another scan began. This scheme underutilized the mechanical bandwidth of our actuation scheme and a substantial fraction of the duty cycle was spent on the slow and wide laser scan.

The second scheme was chosen to maximize the bandwidth of the spectral diffusion correction. Instead of using a direct laser scan, an electro-optic modulator sideband of the excitation laser was scanned using a variable frequency rf source. This scan was much faster compared to the laser scan, potentially allowing for modulation at up to around 100 Hz, limited by the switching time of the rf source. By scanning the EOM sideband over the target position of the SiV spectral line, a similar absorption profile could be generated. By implementing a software lock-in scheme, we were able to rapidly turn this absorption profile into an error signal which could be used to correct the voltage applied to the cantilever.

We note that, at high strain and in a magnetic field aligned to the SiV axis, the SiV spin transitions are to first order insensitive to strain field fluctuations [22]. As a result, high bandwidth stabilization of SiV optical transitions should minimally impact the electron spin levels of the SiV color center. Further, strain does not, to first order, break the inversion symmetry of the SiV [1].

APPENDIX D: EMITTER MODEL AND SIMULATION

In this appendix, we present a model to describe the generation of an entangled state between two SiV centers and the results presented in Fig. 4. We simulated our system through the Lindblad master equation formalism using the QuTiP software package [27]. Each SiV center is governed by a single emitter Hamiltonian defined by

$$H = \omega_e|e\rangle\langle e| + \omega_u|u\rangle\langle u| + \Omega|e\rangle\langle u| + \Omega|u\rangle\langle e|, \quad \text{(D1)}$$

where ω_e is the energy associated with the excited state, ω_u is the energy of the upper branch of the ground state, and Ω corresponds to the driving rate associated with the laser power. In this case the $|e\rangle$ state is the lower spin-orbit branch of the excited state, while $|u\rangle$ and $|c\rangle$ represent the upper and lower branches of the ground state, respectively. Because we operated in the weak driving regime and photons can escape rapidly from our waveguide coupled color centers, we truncated our Hilbert space to

$$|ee\rangle, |ec\rangle, |ce\rangle, |cc\rangle, |eu\rangle, |ue\rangle, |uu\rangle, |uc\rangle, |cu\rangle, \quad \text{(D2)}$$

leading to the states with at most two excitations and 0 photons being included in the simulation. Each individual

emitter was also subjected to a series of collapse operators representing coupling to the environment and incoherent population transfer between energy levels. These took the form of

$$C_1 = \sqrt{w_1}|c\rangle\langle e|, \qquad C_2 = \sqrt{w_2}|u\rangle\langle e|,$$
$$C_3 = \sqrt{w_3}|u\rangle\langle c|, \qquad C_4 = \sqrt{w_4}|c\rangle\langle u|,$$
$$C_5 = \sqrt{w_5}|e\rangle\langle e|, \qquad\qquad\qquad \text{(D3)}$$

which represent, in order, the decay between $|e\rangle$ and $|c\rangle$, the decay between $|e\rangle$ and $|u\rangle$, the ground-state mixing rate (up and down), and the fast spectral diffusion, along with their associated rates. The ground-state mixing is a result of phonon occupation at the 50 GHz energy scale, which occurs at 4 K. Finally, to account for the slow component of the spectral diffusion, the simulation was run repeatedly with the positions of two SiV center spectral lines independently and randomly chosen from a Gaussian distribution. The results of these iterations were then averaged. This enabled us to account for the dynamic effects on the timescale of a single experimental run (fast diffusion, tens of nanoseconds) and variations over the course of a single data collection period (slow diffusion, minutes) in simulations.

The initial state of the system was defined to be the two-emitter steady state, as calculated from the Lindblad formalism. Detection of the first photon corresponds to one application of the relevant collapse operator C_1. In order to calculate the two-emitter $g^{(2)}$, the collapse operators were applied to the system using the definition [6]

$$g^{(2)}(t) = \frac{\text{Tr}\{C_1^\dagger C_1 \tilde{\rho}(t)\}}{\text{Tr}\{C_1^\dagger C_1 \rho\}}. \quad \text{(D4)}$$

Term ρ is the steady-state density matrix of the two-emitter system and $\tilde{\rho}(t)$ represents the density matrix at time t after application of the collapse operator C_1, corresponding to the first photon being detected.

In order to model our experimental system, variables were extracted from our measurements and from the theoretical properties of the SiV centers. We set the average separation between the spectral lines of the two emitters to be 250 MHz, which is half of the filter cavity linewidth (a conservative estimate), and the driving power of the laser was matched between measured and simulated saturation curves such that counts were produced at 2/3 of the saturation rate. Only the ground-state mixing rate was fit to the measured $g^{(2)}$ dip timescale, visible in the red line fit in Fig. 4(c) of the main text. All other parameters could be extracted directly from optical and electrical measurements in our system.

Simulations using these parameters predicted a $g^{(2)}$ curve as shown in Fig. 7. When no model is used to account for the jitter in detection electronics, the peak of the $g^{(2)}(0)$
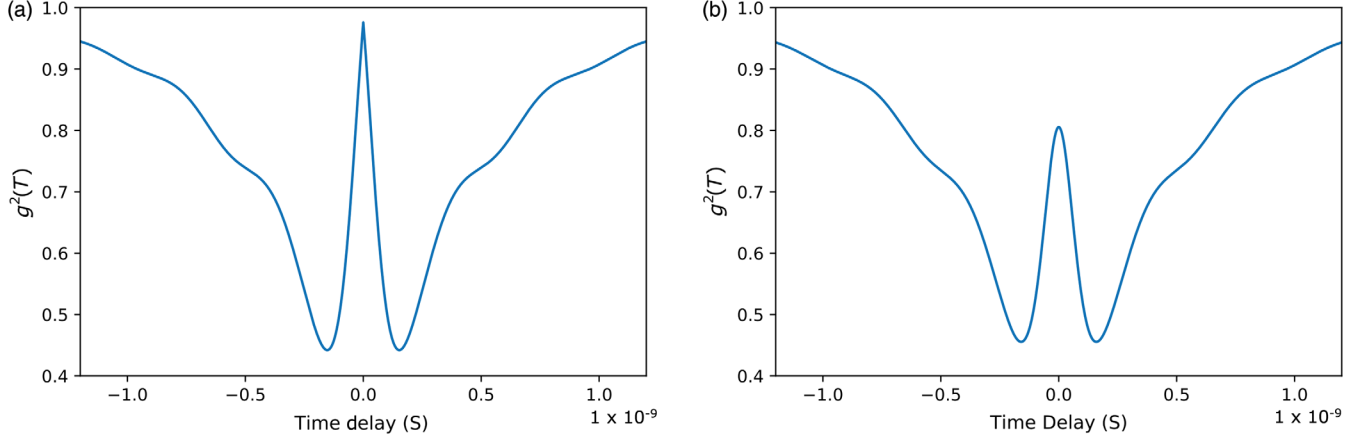
FIG. 7. Simulated photon correlation function for two emitters on resonance without (a) and with (b) inclusion of electronic jitter measured in the experiment.

goes to 1 [Fig. 7(a)]. However, in our system the jitter of the detection electronics was measured to be roughly 350 ps, a substantial fraction of the lifetime of the feature being measured. This jitter was modeled as convolution of the original $g^{(2)}$ signal with a Gaussian of the appropriate width. As a result of this jitter, the peak height of $g^{(2)}(0)$ was reduced to 0.85 [Fig. 7(b)], in good agreement with measured results. Using low jitter detectors in our experiment would increase the contrast of the superradiant feature observed in Fig. 4.

APPENDIX E: BRIGHT-STATE FIDELITY ANALYSIS

A lower bound on the conditional fidelity of the generated bright state can be extracted from the two-photon correlation measurements [6]. We begin by calculating the impact of the avalanche photodiode noise counts on our measurements. In our single emitter photon correlation measurement we observed a nonzero $g^{(2)}(0)$ primarily due to dark counts in our detectors. Considering the possibility that either one or both photons of the coincidence measurement was a noise photon, we found that

$$g_1^{(2)}(0) = \frac{p_{n,1}(2 + p_{n,1})}{(1 + p_{n,1})^2}, \tag{E1}$$

where $g_1^{(2)}(0)$ is the zero-time-delay two-photon correlation measurement for a single emitter and $p_{n,1}$ is the relative probability that a photon measured when exciting a single emitter is a noise photon. In our system $g_1^{(2)}(0) = 0.13(4)$, which results in a $p_{n,1} = 0.07(3)$. Because the dominant source of noise is the detector dark counts, the noise probability was halved in the experiment with two emitters, resulting in $p_n = 0.04(2)$.

In our experiment involving indistinguishable photons emitted from two SiV centers, both emitters were continuously excited and the excitation power was individually set to balance the measured counts from each emitter. For notational simplicity, in this analysis it was assumed that the driving power was weak enough that the admixture of the $|u\rangle$ state into the excited component of the bright state was negligible. As a result, the conditional density matrix for the system after detection of a single photon is

$$\tilde{\rho} = \frac{1}{1 + p_n}[p_e^{(0)}\tilde{F}|B\rangle\langle B| + (1 - p_e^{(0)}\tilde{F})\rho_d] + \frac{p_n}{1 + p_n}\rho, \tag{E2}$$

where $p_e^{(0)}$ represents the probability that an emitter is in the excited state, $\tilde{F}$ represents the fidelity of the bright state if the two SiVs begin in the excited state, ρ_d is the density matrix representing all nonradiative states, and ρ is the steady-state density matrix. The first term of this equation represents the state of the system if the detected photon originated from the excited emitters. The second term represents the case of the photon originating from the detector noise. This density matrix produces a conditional $g^{(2)}$ function of the form

$$g^{(2)}(0) = \frac{\tilde{F} + p_n(2 + p_n)}{(1 + p_n)^2}, \tag{E3}$$

which allows us to extract this conditional fidelity from our photon correlation measurements. In order to introduce our second postselection step, the probability p_c^{ee} that the system started in the doubly excited state given that two photons were detected must be calculated. This can then be used to convert $\tilde{F}$ into the correct conditional fidelity F through the relation $F = \tilde{F}p_c^{ee}$. The probability can be obtained using the relative rates of photon production by emitters and dark counts calculated above:

$$p_c^{ee} \geq \frac{\tilde{F}}{\tilde{F} + p_n(2 + p_n)}. \tag{E4}$$

From this we can calculate a lower bound on the conditional fidelity of

$$F \geq \frac{[g^{(2)}(0)(1+p_n)^2 - p_n(2+p_n)]^2}{g^{(2)}(0)(1+p_n)^2} = 0.8(1). \quad \text{(E5)}$$

This value is limited by the jitter in our detection electronics, indicating that performing measurements with lower jitter would result in substantial improvements in the fidelity of this bright state.

The nature of the bright state generated in this experiment is dependent on the excitation power used. When driven well below saturation, the bright state in this system is defined as the $|B\rangle = (|ec\rangle + |ce\rangle)/\sqrt{2}$ state. Increasing the driving power of the resonant laser increases the admixture of the $|u\rangle$ state into the excited component of the bright state. This does not change the fidelity calculations used but does result in a different definition of the bright state observed.

The creation of the bright state in this system is not fully heralded by detection of a photon due to the three-level structure of the emitters used in this experiment. The probability of finding both emitters simultaneously in the excited state at any given point of time is low: less than 10%, according to the steady-state simulations of the model described above. As a result, detection of the first photon will produce the bright state only a fraction of the time. Calculation of the concurrence conditional on photon collection [6] yields a negligibly small (roughly 0.1σ) concurrence for this experiment. This could be improved by employing a pulsed excitation scheme or using other deterministic schemes for entanglement generation.

[1] C. Hepp, T. Müller, V. Waselowski, J. N. Becker, B. Pingault, H. Sternschulte, D. Steinmüller-Nethl, A. Gali, J. R. Maze, M. Atatüre, and C. Becher, *Electronic Structure of the Silicon Vacancy Color Center in Diamond*, Phys. Rev. Lett. **112**, 036405 (2014).

[2] H.-J. Briegel, W. Dür, J. I. Cirac, and P. Zoller, *Quantum Repeaters: The Role of Imperfect Local Operations in Quantum Communication*, Phys. Rev. Lett. **81**, 5932 (1998).

[3] L.-M. Duan, M. D. Lukin, J. I. Cirac, and P. Zoller, *Long-Distance Quantum Communication with Atomic Ensembles and Linear Optics*, Nature (London) **414**, 413 (2001).

[4] H. J. Kimble, *The Quantum Internet*, Nature (London) **453**, 1023 (2008).

[5] S. Wehner, D. Elkouss, and R. Hanson, *Quantum Internet: A Vision for the Road Ahead*, Science **362**, eaam9288 (2018).

[6] A. Sipahigil, R. E. Evans, D. D. Sukachev, M. J. Burek, J. Borregaard, M. K. Bhaskar, C. T. Nguyen, J. L. Pacheco, H. A. Atikian, C. Meuwly, R. M. Camacho, F. Jelezko, E. Bielejec, H. Park, M. Lončar, and M. D. Lukin, *An Integrated Diamond Nanophotonics Platform for Quantum-Optical Networks*, Science **354**, 847 (2016).

[7] D. D. Sukachev, A. Sipahigil, C. T. Nguyen, M. K. Bhaskar, R. E. Evans, F. Jelezko, and M. D. Lukin, *Silicon-Vacancy Spin Qubit in Diamond: A Quantum Memory Exceeding 10 ms with Single-Shot State Readout*, Phys. Rev. Lett. **119**, 223602 (2017).

[8] R. E. Evans, A. Sipahigil, D. D. Sukachev, A. S. Zibrov, and M. D. Lukin, *Narrow-Linewidth Homogeneous Optical Emitters in Diamond Nanostructures via Silicon Ion Implantation*, Phys. Rev. Applied **5**, 044010 (2016).

[9] R. E. Evans, M. K. Bhaskar, D. D. Sukachev, C. T. Nguyen, A. Sipahigil, M. J. Burek, B. Machielse, G. H. Zhang, A. S. Zibrov, E. Bielejec, H. Park, M. Lončar, and M. D. Lukin, *Photon-Mediated Interactions between Quantum Emitters in a Diamond Nanocavity*, Science **362**, 662 (2018).

[10] W. B. Gao, A. Imamoglu, H. Bernien, and R. Hanson, *Coherent Manipulation, Measurement and Entanglement of Individual Solid-State Spins Using Optical Fields*, Nat. Photonics **9**, 363 (2015).

[11] M. J. Burek, C. Meuwly, R. E. Evans, M. K. Bhaskar, A. Sipahigil, S. Meesala, B. Machielse, D. D. Sukachev, C. T. Nguyen, J. L. Pacheco, E. Bielejec, M. D. Lukin, and M. Lončar, *Fiber-Coupled Diamond Quantum Nanophotonic Interface*, Phys. Rev. Applied **8**, 024026 (2017).

[12] P. Udvarhelyi, R. Nagy, F. Kaiser, S.-Y. Lee, J. Wrachtrup, and A. Gali, *Spectrally Stable Defect Qubits with No Inversion Symmetry for Robust Spin-to-Photon Interface*, Phys. Rev. Applied **11**, 044022 (2019).

[13] T. Zhong, J. M. Kindem, J. G. Bartholomew, J. Rochman, I. Craiciu, V. Verma, S. W. Nam, F. Marsili, M. D. Shaw, A. D. Beyer, and A. Faraon, *Optically Addressing Single Rare-Earth Ions in a Nanophotonic Cavity*, Phys. Rev. Lett. **121**, 183603 (2018).

[14] D. D. Awschalom, R. Hanson, J. Wrachtrup, and B. B. Zhou, *Quantum Technologies with Optically Interfaced Solid-State Spins*, Nat. Photonics **12**, 516 (2018).

[15] P. Lodahl, *Scaling Up Solid-State Quantum Photonics*, Science **362**, 646 (2018).

[16] P. Tamarat, T. Gaebel, J. R. Rabeau, M. Khan, A. D. Greentree, H. Wilson, L. C. L. Hollenberg, S. Prawer, P. Hemmer, F. Jelezko, and J. Wrachtrup, *Stark Shift Control of Single Optical Centers in Diamond*, Phys. Rev. Lett. **97**, 083002 (2006).

[17] S. Sun, J. L. Zhang, K. A. Fischer, M. J. Burek, C. Dory, K. G. Lagoudakis, Y.-K. Tzeng, M. Radulaski, Y. Kelaita, A. Safavi-Naeini, Z.-X. Shen, N. A. Melosh, S. Chu, M. Lončar, and J. Vučković, *Cavity-Enhanced Raman Emission from a Single Color Center in a Solid*, Phys. Rev. Lett. **121**, 083601 (2018).

[18] S. Sun, H. Kim, G. S. Solomon, and E. Waks, *Strain Tuning of a Quantum Dot Strongly Coupled to a Photonic Crystal Cavity*, Appl. Phys. Lett. **103**, 151102 (2013).

[19] M. Zopf, T. Macha, R. Keil, E. Uruñuela, Y. Chen, W. Alt, L. Ratschbacher, F. Ding, D. Meschede, and O. G. Schmidt, *Frequency Feedback for Two-Photon Interference from Separate Quantum Dots*, Phys. Rev. B **98**, 161302(R) (2018).

[20] S. Meesala, Y.-I. Sohn, B. Pingault, L. Shao, H. A. Atikian, J. Holzgrafe, M. Gündoğan, C. Stavrakas, A. Sipahigil, C. Chia, R. Evans, M. J. Burek, M. Zhang, L. Wu, J. L. Pacheco, J. Abraham, E. Bielejec, M. D. Lukin, M. Atatüre, and M. Lončar, *Strain Engineering of the Silicon-Vacancy Center in Diamond*, Phys. Rev. B **97**, 205444 (2018).

[21] Y.-I. Sohn, S. Meesala, B. Pingault, H. A. Atikian, J. Holzgrafe, M. Gündogan, C. Stavrakas, M. J. Stanley, A. Sipahigil, J. Choi, M. Zhang, J. L. Pacheco, J. Abraham, E. Bielejec, M. D. Lukin, M. Atatüre, and M. Loncar, *Controlling the Coherence of a Diamond Spin Qubit through Its Strain Environment*, Nat. Commun. **9,** 2012 (2018).

[22] M. J. Burek, Y. Chu, M. S. Z. Liddy, P. Patel, J. Rochman, S. Meesala, W. Hong, Q. Quan, M. D. Lukin, and M. Loncar, *High Quality-Factor Optical Nanocavities in Bulk Single-Crystal Diamond*, Nat. Commun. **5,** 5718 (2014).

[23] H. A. Atikian, P. Latawiec, M. J. Burek, Y.-I. Sohn, S. Meesala, N. Gravel, A. B. Kouki, and M. Lonar, *Free-standing Nanostructures via Reactive Ion Beam Angled Etching*, APL Photonics **2,** 051301 (2017).

[24] D. M. Toyli, C. D. Weis, G. D. Fuchs, T. Schenkel, and D. D. Awschalom, *Chip-Scale Nanofabrication of Single Spins and Spin Arrays in Diamond*, Nano Lett. **10,** 3168 (2010).

[25] P. Ovartchaiyapong, K. W. Lee, B. A. Myers, and A. C. B. Jayich, *Dynamic Strain-Mediated Coupling of a Single Diamond Spin to a Mechanical Resonator*, Nat. Commun. **5,** 4429 (2014).

[26] M. Gross and S. Haroche, *Superradiance: An Essay on the Theory of Collective Spontaneous Emission*, Phys. Rep. **93,** 301 (1982).

[27] J. Johansson, P. Nation, and F. Nori, *QuTiP 2: A Python Framework for the Dynamics of Open Quantum Systems*, Comput. Phys. Commun. **184,** 1234 (2013).

[28] S. Maity, L. Shao, Y.-I. Sohn, S. Meesala, B. Machielse, E. Bielejec, M. Markham, and M. Lončar, *Spectral Alignment of Single-Photon Emitters in Diamond Using Strain Gradient*, Phys. Rev. Applied **10,** 024050 (2018).

[29] J. Majer, J. M. Chow, J. M. Gambetta, J. Koch, B. R. Johnson, J. A. Schreier, L. Frunzio, D. I. Schuster, A. A. Houck, A. Wallraff, A. Blais, M. H. Devoret, S. M. Girvin, and R. J. Schoelkopf, *Coupling Superconducting Qubits via a Cavity Bus*, Nature (London) **449,** 443 (2007).

[30] M.-A. Lemonde, S. Meesala, A. Sipahigil, M. J. A. Schuetz, M. D. Lukin, M. Loncar, and P. Rabl, *Phonon Networks with Silicon-Vacancy Centers in Diamond Waveguides*, Phys. Rev. Lett. **120,** 213603 (2018).

[31] M. J. Burek, N. P. de Leon, B. J. Shields, B. J. M. Hausmann, Y. Chu, Q. Quan, A. S. Zibrov, H. Park, M. D. Lukin, and M. Loncar, *Free-Standing Mechanical and Photonic Nanostructures in Single-Crystal Diamond*, Nano Lett. **12,** 6084 (2012).

[32] J. F. Ziegler, M. Ziegler, and J. Biersack, *SRIM—The Stopping and Range of Ions in Matter (2010)*, Nucl. Instrum. Methods Phys. Res., Sect. B **268,** 1818 (2010).

[33] J. N. Becker and C. Becher, *Coherence Properties and Quantum Control of Silicon Vacancy Color Centers in Diamond*, Phys. Status Solidi A **214,** 1770170 (2017).